

Imaging Breast Microcalcifications Using Dark-Field Signal in Propagation-Based Phase-Contrast Tomography

A. Aminzadeh¹, B. D. Arhatari, A. Maksimenko, C. J. Hall², D. Hausermann, A. G. Peele, J. Fox³, B. Kumar, Z. Prodanovic, M. Dimmock⁴, *Member, IEEE*, D. Lockie, K. M. Pavlov⁵, Y. I. Nesterets⁶, D. Thompson, S. C. Mayo, D. M. Paganin⁷, S. T. Taba⁸, S. Lewis, P. C. Brennan, H. M. Quiney, and T. E. Gureyev⁹

Abstract—Breast microcalcifications are an important primary radiological indicator of breast cancer. However, microcalcification classification and diagnosis may be still challenging for radiologists due to limitations of the standard 2D mammography technique, including spatial and contrast resolution. In this study, we propose an approach to improve the detection of microcalcifications in propagation-based phase-contrast X-ray computed tomography of breast tissues. Five fresh mastectomies containing microcalcifications were scanned at different X-ray energies and radiation doses using synchrotron radiation. Both bright-field (i.e. conventional phase-retrieved images) and dark-field images were extracted from the same data sets using different image processing methods. A quantitative analysis was performed in terms of visibility and contrast-to-noise ratio of microcalcifications. The results show that while the signal-to-noise and the contrast-to-noise ratios are lower, the visibility of the microcalcifications is more than two times higher in the dark-field images compared to the bright-field images. Dark-field images have also provided more accurate information about the size and shape of the microcalcifications.

Index Terms—Breast cancer, dark-field imaging, microcalcifications, propagation-based phase-contrast CT, X-ray imaging.

I. INTRODUCTION

BREAST cancer is one of the most common cancers worldwide and the leading cause of cancer-related death in women [1]. The number of new cases is increasing each year while the rate of mortality is slightly decreasing [2], which is mainly due to the improvements in treatments as well as

Manuscript received 14 March 2022; revised 6 May 2022; accepted 10 May 2022. Date of publication 18 May 2022; date of current version 27 October 2022. This work was supported in part by the Australian National Breast Cancer Foundation under Grant IN-16-001; in part by the National Health and Medical Research Council (NHMRC), Australia, under Grant APP1138283; and in part by Australia's Nuclear Sciences and Technology Organisation (ANSTO) Project Funding. (*Corresponding author: A. Aminzadeh.*)

This work involved human subjects or animals in its research. Approval of all ethical and experimental procedures and protocols was granted by the Human Ethics Certificate of Approval from Monash University under Application No. 26399.

Please see the Acknowledgment section of this paper for the author affiliations.

Digital Object Identifier 10.1109/TMI.2022.3175924

early detection of breast cancer through screening programs such as mammography. One of the most important primary radiological signs in the early detection of breast cancer is the presence of microcalcifications within the breast [3], [4]. Microcalcifications are small deposits of calcium salts that can be detected by X-ray imaging. In conventional attenuation-based X-ray mammography, the standard method for breast cancer imaging, microcalcifications appear as hyperdense foci within a breast image due to having a much higher X-ray attenuation (compared to the neighboring tissues). The sizes and shapes of microcalcifications, as well as their positions within the breast, can indicate benign or malignant manifestations. The morphologies and distributions (clustered or segmented) of microcalcifications are also important in their classification [3]. Hence, an essential goal in diagnostic imaging is to detect microcalcifications and resolve their morphology. Unfortunately, microcalcification diagnosis may be still challenging for radiologists due to limitations of standard 2D mammography [5]. Current clinical mammography techniques can only reliably resolve a few types of microcalcification configurations, with other configurations remaining unresolved [3], [4], resulting in the need for additional biopsies. There is also some controversy regarding the existence of any benefit with Digital Breast Tomosynthesis (DBT) for malignant calcifications, compared with conventional mammography [6].

Multiple algorithms and image processing methods have been implemented to improve the detection of microcalcifications in mammograms [7]–[12]. However, there are still large numbers of false positive and false negative cases after applying those approaches. Furthermore, most of these approaches are less efficient for dense breast tissue which can mask the appearance of microcalcifications [8].

Computed Tomography (CT) is an X-ray imaging technique that provides a full 3D image of an object [13]. There are different types of CT techniques. One of these techniques is polyenergetic cone-beam breast CT in which an X-ray tube and a detector are rotated around a breast tissue (which is hanging freely) and the projections are collected in a single scan [14]. The outcome is true 3D images of a breast tissue that can be superior to 2D mammography as it removes tissue overlap and creates cross-sectional slices of a breast with higher contrast-to-noise ratio (CNR), improving diagnostic accuracy

especially for dense breast tissues. It has also shown high accuracy for quantitative volumetric breast density (QVBD) measurements [15]. Another advantage of cone-beam CT in breast imaging (over 2D mammography) is that this technique does not require painful compression of the breast [14], [16]. However, it has a lower spatial resolution compared to digital mammography [14], [17].

Spiral breast CT is a more recent technique, which is similar to cone-beam CT but can offer higher spatial resolution compared to mammography [17]. Recent implementations of this technique use a photon counting detector instead of a flat panel detector, which improves the quality of images. Spiral breast CT has also shown better microcalcification visualization compared to mammography and cone-beam CT [17], [18].

A different and promising CT imaging technique, which recently has attracted a lot of attention in breast cancer imaging [19]–[22], is phase-contrast CT. This method is capable of producing high-contrast images of materials with similar X-ray attenuation coefficients, such as different types of soft tissues in the breast [23]. The technique uses refraction of X-rays to enhance the visibility of boundaries between different materials within an object. In this study, we employed propagation-based phase-contrast CT (PB-CT) X-ray imaging [24], which was proved to provide a higher image quality (in breast cancer imaging) compared to cone-beam CT [25]. PB-CT images of a phantom have also shown a higher signal-to-noise ratio (SNR) and spatial resolution as well as better calcification visualization compared to images obtained from clinical breast CT [26]. Moreover, Mettievier *et al.* have recently developed a PB micro-CT scanner that uses a microfocus X-ray tube and a high-resolution flat-panel detector (with a pixel pitch of 50 μm) to improve the visibility of microcalcifications. In a study performed with a breast phantom, they reported an improvement in microcalcification and mass visibility after applying a phase retrieval technique [27]. Another advantage of the PB-CT technique is that, unlike other popular phase-contrast CT techniques, such as analyser-based [28], edge-illumination [29] and grating-based CT [23], PB-CT does not require any additional optical elements to be used for image formation. However, a high degree of spatial coherence of the incident beam is important in PB-CT to achieve significant phase-contrast in the images. When a spatially coherent X-ray beam passes through an object, the wavefront is distorted, and the phase of the X-ray beam changes as a result. These phase variations are then transformed into detectable intensity contrast as the beam propagates in free space towards a detector, which is placed at some distance away from the object [30]. The object-to-detector distance (also called the propagation distance) should be large enough to create detectable phase contrast in free-space propagation. Brombal *et al.* studied the effect of propagation distance on the image quality in PB-CT breast imaging and demonstrated a significant increase in SNR at the same spatial resolution, by increasing the propagation distance from 1.6 m to 9 m [31]. Piai *et al.* reported accurate measurements of the attenuation coefficient of breast tissues, which were fixed in formalin, using a synchrotron based PB-CT technique [32].

Detectors can only record the intensity of X-rays but not the phase. The phase distribution can then be reconstructed from the registered intensity using suitable mathematical algorithms. One of the most effective algorithms used in PB-CT is called TIE-Hom, which is based on the Transport of Intensity equation (TIE) [33] but is modified for homogeneous objects (having the same ratio of real to imaginary parts of the complex refractive index throughout an object) [34]. More information about the TIE-Hom algorithm is provided in Section II.B. In addition to collecting phase-contrast images (which are also called bright-field images in this context for the reasons explained below), dark-field images can be obtained from the same data sets. Dark-field images are particularly sensitive to sharp small features and also boundaries between different components in the imaged object. Dark-field images can also visualize small angle scattering (SAXS) signals, which have shown the potential to improve visualization, as well as classification, of microcalcifications in human breasts [3], [35], [36].

Frappart *et al.* reported two main types of breast microcalcifications: type one (I) consists of weddellite crystals ($\text{CaC}_2\text{O}_4 \cdot 2\text{H}_2\text{O}$), which are usually seen in benign lesions and are rarely associated with breast cancer, and type two (II) consists of calcium hydroxyapatite ($\text{Ca}_5(\text{PO}_4)_3(\text{OH})$), which are found in both benign and malignant lesions and are often associated with breast cancer [37]. Wang *et al.* collected both dark-field and bright-field images of human breasts using a grating interferometer and classified breast microcalcifications based on their chemical composition [4]. They have concluded that type one (I) microcalcifications have lower X-ray absorption and higher scattering signals compared to type two (II) microcalcifications [4]. Scherer *et al.* have also shown that dark-field images collected with a grating interferometer can improve microcalcification assessments in breast cancer diagnosis [3]. They have categorized microcalcifications into four microstructure classes based on their micromorphology rather than chemical composition [3]. Ultra-fine and fine microstructures, which are mostly associated with benign microcalcifications, have shown higher scattering signals and lower absorption contrast compared to coarse microstructures, which are mostly associated with malignant microcalcifications. The use of X-ray grating interferometers in these studies made the data collection more complicated compared to conventional mammography and breast CT.

The present paper builds upon our previous work on dark-field PB X-ray imaging [36], which does not require any additional X-ray optical elements such as interferometers. Here, we develop a new and more efficient algorithm for extraction of the dark-field signal from PB images and apply it to the analysis of PB-CT scans of five fresh mastectomies containing microcalcifications. The scans were collected using monochromatic synchrotron radiation. Both bright-field and dark-field images were extracted from the collected data. The visibility and CNR of the microcalcifications in bright-field and dark-field images were assessed at different X-ray energies and radiation doses, allowing us to evaluate the potential of the dark-field PB-CT technique for imaging breast microcalcifications.

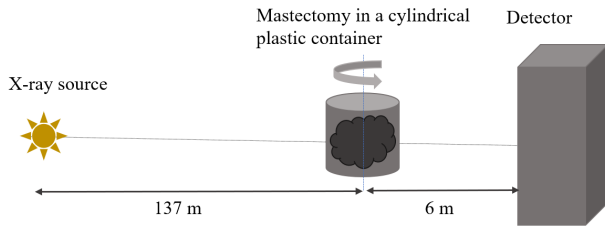


Fig. 1. Schematic diagram of the experimental setup.

II. MATERIALS AND METHODS

A. Experimental Setup and Sample Preparation

The propagation-based phase-contrast CT experiments were performed at the Imaging and Medical beamline (IMBL) of the Australian Synchrotron. A schematic diagram of the experimental setup is shown in Fig. 1. Relevant details about the main IMBL components and geometries can be found in Stevenson *et al.* [38].

Five fresh whole mastectomies containing microcalcifications were scanned with a monochromatic beam having a band pass of approximately 0.2 keV, at X-ray energies of 32 keV and 34 keV, and mean glandular doses (MGD) of 4 mGy, 8 mGy, and 24 mGy. These X-ray imaging parameters have been shown to produce high-quality PB-CT images in our previous optimisation studies [3], [24]–[40]. The MGD was calculated from photon fluence that was measured by an ion chamber, which was placed in the X-ray beam before the sample. This photon fluence was then converted to MGD using both Monte Carlo and analytic calculations in the same way as reported in our previous publication [41]. The first three mastectomy samples were imaged using a Hamamatsu C10900D Flat Panel Sensor detector with a pixel pitch of 100 μm and frame rate of 17 fps. For the two other mastectomy samples, a Teledyne-Dalsa Xineos-3030HR detector with a pixel pitch of 99 μm , and frame rate of 54 fps was used. The spatial resolution of the PB-CT imaging setup with both of these detectors was approximately 170 μm [42]. A region of interest (ROI) with an area of approximately 150 mm \times 40 mm (horizontal \times vertical) was created on the detector. The width of the ROI was chosen to be slightly larger than the width of our breast tissue containers and the height of the ROI was limited by the height of the X-ray beam. For the specimens that were larger than the height of the ROI in the vertical direction, multiple scans were performed at different positions by moving the specimen stage in the vertical direction with respect to the detector. The sample-to-detector distance was 6 m, which was the maximum possible free-space propagation distance that we could obtain at the IMBL [38].

The imaging experiment was conducted under a Human Ethics Certificate of Approval from Monash University (project no. 26399) and with written consent from the patients to image their clinical specimens. The patients were all females. Each specimen was a full-size human mastectomy, imaged only a few hours after the surgery. No preservation or cutting of the specimens was performed prior to the X-ray scans, in an attempt to approximate the anticipated

TABLE I
INFORMATION ABOUT THE MASTECTOMY SAMPLES

Sample ID	Patient age (yrs)	Sample weight (g)	Diagnosis
1	73	802	High grade DCIS with central necrosis and calcification; Invasive carcinoma, no special type.
2	40	295	High grade DCIS; no invasive tumour.
3	53	832	High grade DCIS; no invasive tumour.
4	69	669	Grade 2 invasive carcinoma.
5	54	390	Invasive tumour: invasive carcinoma, no special type. BRE (Bloom–Richardson–Elston system) Grade 2. In-situ tumour: extensive high grade DCIS with solid and cribriform architectures; with extensive luminal necrosis and calcification.

in vivo imaging conditions. Four out of five mastectomies contained ductal carcinoma in situ (DCIS), and the remaining sample contained an invasive carcinoma. Essential information about the mastectomy samples is summarised in Table I. The mastectomies were scanned in an 11 cm (in diameter) thin-walled plastic container. Each scan contained 4,800 projections collected over 180 degrees, with a rotation step of 0.0375 degrees. In addition, 100 images of the flat field (i.e. the images collected by the detector in the presence of the incident beam without having a specimen in the beam) and 100 images of the detector background or dark-current (i.e. the images collected by the detector in the absence of the incident beam) were also collected before each scan. The scan time was approximately 5 minutes for each CT scan at a fixed vertical position of the sample. Most samples required between two and five such scans at different vertical positions in order to image the whole sample. Note that in the PB-CT breast imaging of live patients at the Imaging and Medical Beamline of the Australian Synchrotron the beam height will be increased and a different, significantly faster detector will be used. This will allow the scan time (not including the acquisition of dark-current and flat-field images which will be collected separately, if needed) to be reduced to approximately 15–20 seconds, during which a patient could comfortably hold their breath. This will help to minimize movement artefacts in PB-CT imaging of live patients.

B. Image Reconstruction Methods

The PB-CT image reconstruction method used in this study can be logically divided into three steps. The first step was to

stitch multiple projections, which were collected in multiple series (in the vertical direction), after flat-field and dark-current corrections. The second step was to extract “bright-field” images using the TIE-Hom algorithm in combination with conventional CT reconstruction. Conventional Filtered Back Projection (FBP) was used for the CT reconstruction step in our work [41]. The third step was to extract dark-field signals from the same data sets using the first Born approximation technique, followed by conventional CT reconstruction. These steps are further explained below.

TIE-Hom is a well-known phase retrieval technique (also known as Paganin’s method [34]) that utilizes both absorption and refraction of the X-ray beam to increase the CNR in the images, which is essential when imaging soft tissues at low doses. A comprehensive description of TIE-Hom along with relevant mathematics can be found in the literature [34]. The key parameter in this technique is γ that defines the ratio between the real decrement (δ) and the imaginary (β) part of the complex refractive index $n = 1 - \delta + i\beta$, i.e. $\gamma = \delta/\beta$. Here, δ and β depend on the radiation wavelength (or X-ray energy) and are related to the phase shift and absorption of a material (breast tissues in our case), respectively. For breast tissues, the mean γ values were calculated as 550 and 600 at 32 keV and 34 keV, respectively. These theoretical values are based on the complex refractive index of glandular tissue with respect to blood. However, in our previous study [40], we have shown that the overall PB-CT image quality is maximized when using approximately twice smaller values for γ in the TIE-Hom algorithm when imaging mastectomy samples. Thus, the corresponding practical γ values (called γ_1 in (2) below) used in this study were 275 and 300, at 32 keV and 34 keV, respectively, allowing us to extract high-quality phase-contrast images using the TIE-Hom algorithm.

To obtain dark-field images, we must eliminate the low-order diffraction beams from the intensity registered by the detector. The registered intensities initially contain both bright-field (low-order diffraction) and dark-field (high-order diffraction) information [36], [43], [44]. In Fourier space, this can be represented as [36]

$$\widehat{I}_R(u, v) = \widehat{I}_{R,TIE}(u, v) + \widehat{I}_{R,dark}(u, v), \quad (1)$$

where $\widehat{I}_R(u, v)$ is the Fourier transform of the intensity distribution in the experimental image, $\widehat{I}_{R,TIE}(u, v)$ is the bright-field component, $\widehat{I}_{R,dark}(u, v)$ is the dark-field component, R is the propagation distance, the overhead hat symbol represents the 2D Fourier transform with respect to transverse coordinates x and y , and u, v denote Fourier-space coordinates dual to x and y . The first term on the right-hand side of (1) corresponds to the TIE approximation (which is associated with the bright-field signal) and the second term corresponds to the dark-field signal. We will treat the dark-field signal in the Born approximation, which is justified by the fact that this signal is usually much weaker than the bright-field signal [36], [45]. From a physical perspective, the first term on the right-hand side of (1) corresponds to spatially slowly-varying structure in the sample that is well resolved by the position-sensitive detector; the second term corresponds to sharp interfaces and fine structure in the sample that may be too small to

be directly resolved, but nevertheless influences the measured intensity data on account of the position-dependent SAXS fans that result from X-ray scattering by such microstructures. The bright-field (TIE) signal in the object plane, $R = 0$, in the case of specimens consisting predominantly of a quasi-homogeneous material, is defined as [34], [36]

$$\widehat{I}_{0,TIE}(u, v) = \widehat{I}_R(u, v)/[1 + \gamma_1\pi\lambda R(u^2 + v^2)]. \quad (2)$$

After obtaining $\widehat{I}_{0,TIE}(u, v)$, the bright-field component of the image, $\widehat{I}_{R,TIE}(u, v)$, is calculated by numerical free-space forward propagation, i.e. evaluating the Fresnel diffraction integral, of the homogeneous complex amplitude with the intensity $I_{0,TIE}(x, y)$ and the phase $\varphi_{0,TIE}(x, y) = 0.5\gamma_1 \ln[I_{0,TIE}(x, y)]$. The m -th order Born approximation, $m = 1, 2, \dots$, for the dark-field signal in the object plane can then be evaluated iteratively:

$$\begin{aligned} \widehat{I}_{0,dark}^{(m)}(u, v) &= \widehat{I}_{0,dark}^{(m-1)}(u, v) \\ &+ \frac{\Delta I_{R,dark}^{(m)}(u, v)}{2[\cos[\pi\lambda R(u^2 + v^2)] + \gamma_2 \sin[\pi\lambda R(u^2 + v^2)]]}, \end{aligned} \quad (3)$$

with

$$\Delta \widehat{I}_{R,dark}^{(m)}(u, v) = \widehat{I}_R(u, v) - \widehat{I}_{R,TIE}(u, v) - \widehat{I}_{R,dark}^{(m-1)}(u, v). \quad (4)$$

Here $\widehat{I}_{R,dark}^{(m-1)}(u, v)$ is obtained by numerical free-space forward propagation of the homogeneous complex amplitude with the intensity $I_{0,dark}^{(m-1)}(x, y)$ and the phase $\varphi_{0,dark}^{(m-1)}(x, y) = 0.5\gamma_2 \ln[I_{0,dark}^{(m-1)}(x, y)]$. Note that $\widehat{I}_{0,dark}^{(0)}(u, v) = 0$ by definition, which implies that $\widehat{I}_{R,dark}^{(0)}(u, v) = 0$ as well. Here, γ_2 is again the ratio between the real decrement (δ) and imaginary (β) part of the complex refractive index, however it is allowed to have a different value from γ_1 used in the TIE-Hom approximation. As shown in [36], $\mu_{Born}^{(m)} \equiv I_{0,dark}^{(m)}/I_{0,TIE}$ represents the source of the dark-field signal that is associated with sharp interfaces and spatially-unresolved fine-scale variations in the projected linear attenuation coefficient of the sample. The iterations (3)-(4) can be stopped when the root-mean-square (RMS) norm of the dark-field image increment recovered at the current iteration, $\Delta I_{R,dark}^{(m)}(x, y)$, becomes smaller than the RMS norm of the noise in the original image. The stoppage criterion can be either applied globally for the whole image, or within a selected ROI. An alternative stoppage criterion (explained below) can be based on the initial point of divergence of the iterative process. A flow-chart of this dark-field extraction algorithm is shown in Fig. 2.

The algorithm for dark-field signal extraction from PB-CT projections defined by (2)-(4) is an extension of the non-iterative algorithm of a similar type published earlier [36]. As usual for the Born approximation in perturbation-type numerical methods, the iterative algorithm based on (2)-(4) has a semi-convergent behavior for any realistic input image data containing noise and measurement errors. Therefore, the iterations have to be interrupted at the “optimal” point before

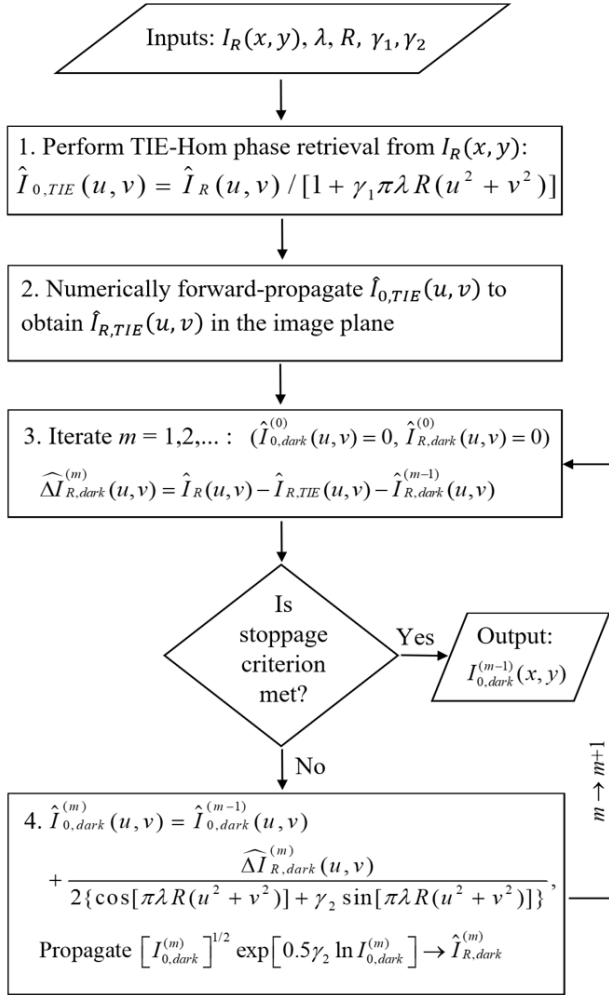


Fig. 2. Flow-chart of the iterative PB-CT dark-field signal extraction method.

the algorithm starts to diverge. In the case of the experimental data analyzed below, it was found that the optimal number of iterations (before the algorithm started to diverge and produce reconstruction artefacts) was $m = 3$. This number can certainly be different in other applications, depending on the noise level in the input data and other relevant factors. The point at which the algorithm starts to diverge is fairly easy to detect in practice, e.g. by evaluating the least-squares norm of (4) at each iteration. When tested on the experimental PB-CT data collected with fresh mastectomy samples as described below, the new algorithm based on (2)-(4) has shown higher spatial resolution (up to 4.3%) and higher microcalcification visibility (up to 16%). Most remarkably, the new algorithm has resulted in higher CNR values (up to 35%) in the dark-field images compared with the results obtained for the same image features using the non-iterative algorithm described in [36]. A universal estimate of the quantitative advantage delivered by the new algorithm, compared to the algorithm published in [36], cannot be given in a general context. Such advantage will always depend on the anatomy of the imaged sample,

as well as on the imaging conditions (such as the X-ray energy, the dose, etc.).

Note that the right-hand side of (4) is equal to $\hat{I}_R(u, v) - \hat{I}_{R,TIE}(u, v)$ at the first iteration, $m = 1$, which represents a measure of the discrepancy between the actual propagation-based phase-contrast image that is measured, and the propagation-based phase-contrast image that would have been measured had no microstructure-induced position-dependent SAXS fans (dark-field signal) and sharp interfaces been present. Indeed, it is precisely the “discrepancy signal,” in the right-hand side of (4), that is the “input” which this algorithm takes in order to compute a dark-field image that is a function of the sharp interfaces and spatially unresolved microstructure. In particular, the aim of extracting dark-field images in this work is to visualize microcalcifications within breast tissue. Thus, the γ_2 value for dark-field images was calculated based on the complex refractive index of calcium in an adipose background at a particular X-ray energy. The γ_2 values used in our dark-field signal extraction were 70.5 and 79 at 32 keV and 34 keV, respectively.

Overall, the process of reconstructing the dark-field images for each projection included the following steps.

1) Phase retrieval from the stitched projections using the TIE-Hom approximation, according to (2). This provides the amplitude, $I_{0,TIE}^{1/2}$, and the phase, $\varphi_{0,TIE} \equiv \gamma_1 \ln I_{0,TIE}^{1/2}$, of the bright-field component of the complex wavefield in the object plane, $z = 0$.

2) Numerical free-space propagation of the complex amplitude, $I_{0,TIE}^{1/2} \exp(i\varphi_{0,TIE})$ (obtained at step 1), to the detector plane $z = R$ by computing the relevant Fresnel integrals.

3) Subtraction of the forward-propagated TIE-Hom intensity, $I_{R,TIE}$, from the original intensity collected at the detector plane. The remaining intensity corresponds to the dark-field signal.

4) Application of the first Born approximation according to (3)-(4) with $m = 1$. The process is then iterated according to (3)-(4) with $m = 2, 3$, as explained above.

After applying the PB-CT reconstruction methods, we obtained a stack of bright-field and a stack of dark-field slices in the coronal view (which corresponded to our experimental layout). The thickness of each slice was 100 μm (corresponding to the pixel size of the detector). The images were then numerically resliced into the sagittal view [40] as was required for radiographic assessments. Maximum Intensity Projection (MIP) of every consecutive subset of 10 sagittal slices (of both bright-field and dark-field images) was also applied to obtain 1 mm thick slices, which was close to the slice thickness in the standard digital breast tomosynthesis [40].

III. RESULTS

Comparing the reconstructed bright-field and dark-field slices, the first noticeable result was the visibility of the microcalcifications in the original reconstructed images (i.e. images without adjustment of the histogram). Fig. shows an example of the microcalcification visibility in bright-field and dark-field images. Fig. 3 (a) and (b) represent original bright-field

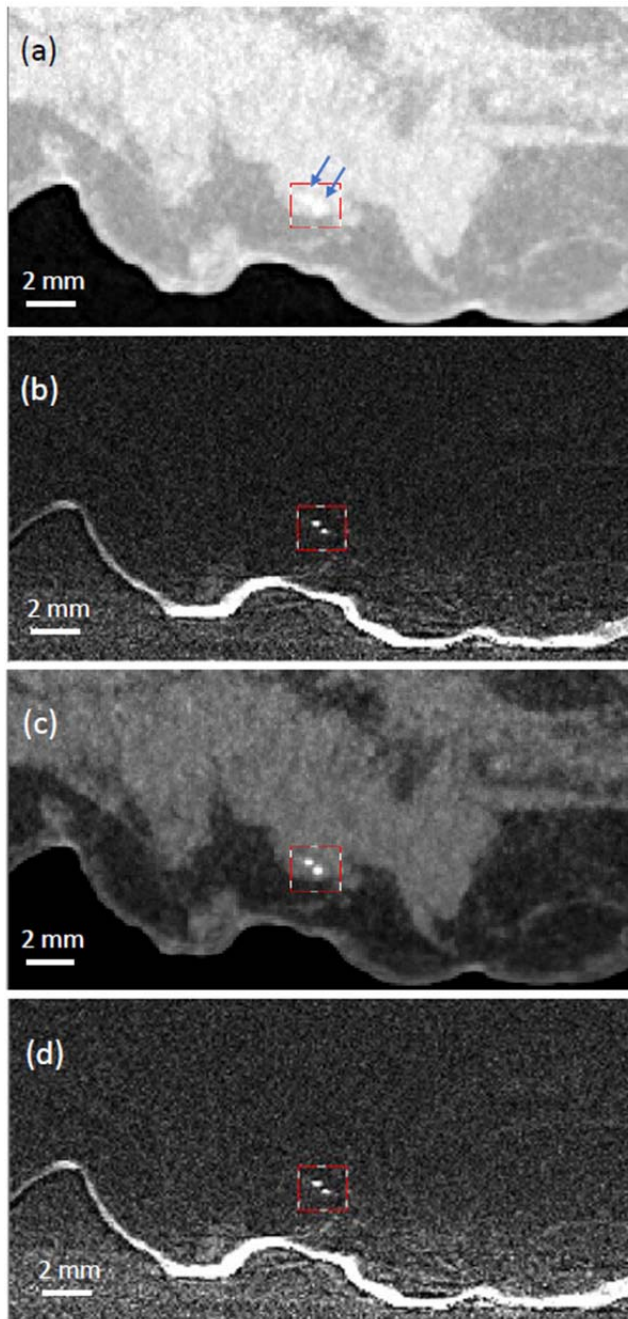


Fig. 3. PB-CT reconstructed images of a sagittal slice of sample 3. The data were collected at 32 keV and 8 mGy radiation dose. (a) and (b) are respectively the original bright-field and dark-field images. (c) and (d) are the same images as (a) and (b) respectively, but after adjustment of the histograms to maximize the visibility of the microcalcifications. Two microcalcifications are outlined with red boxes, which are located at the same position in all images.

and dark-field images, respectively. As can be seen from the images, the two microcalcifications within the red box are more visible in the dark-field image (Fig. 3 (b)) compared to the bright-field image (Fig. (a)). Fig. (c) and (d) are the same images as Fig. (a) and (b), respectively, but after adjustment of the histogram in a manner that maximized the visibility of the microcalcifications. In this case (i.e. after adjusting the histogram), the two microcalcifications can also be seen clearly in the bright-field image as shown in Fig. 3 (c).

Beside the visual assessment, we have also quantitatively measured the visibility of microcalcifications in the reconstructed bright-field and dark-field images at different X-ray energies and radiation doses. Note that the bright-field images were normalized (according to the known physical parameters of the image acquisition and reconstruction) in such a way that the reconstructed pixel values corresponded to the local value of the imaginary part β of the refraction coefficient [46]. In the reconstructed dark-field slices, the average pixel value in “flat” areas not containing any sharp features, such as microcalcifications, was consistently close to zero, in agreement with the fact that there were no sources of dark-field signals in these areas. The latter factor naturally led to high values of visibility and contrast measured in accordance with the conventional approaches as described below.

The measurements were carried out for both coronal and sagittal slices in image areas containing a single microcalcification. A box was defined around a microcalcification and all the pixel values within the box were classified into five equally-sized histogram bins, depending on the pixel values (from the highest pixel values in the first bin to the lowest pixel values in the fifth bin). The visibility V was then calculated as

$$V = (\beta_{hi} - \beta_{low}) / (2\beta_{aver}), \quad (5)$$

where β_{hi} and β_{low} are the average values in the first and last histogram bins (corresponding to the largest and the smallest pixel values, respectively), and β_{aver} is the average of all pixel values within the selected box. Note that the visibility defined in (5) is dimensionless. The results of the visibility measurements are given in Table II. Each visibility value shown in the table is an average of the visibilities of ten individual microcalcifications (calculated using (5)) within the mastectomy sample, in coronal and sagittal slices, as indicated. Note that the same microcalcifications were chosen in the dark-field and bright-field slices.

In addition to the microcalcification visibility, we also measured CNR for the same microcalcifications as selected for the visibility study. The CNR was defined here as a product of visibility and SNR ($CNR = V \times SNR$), with the SNR defined as

$$SNR = \beta_{aver} / \sigma, \quad (6)$$

where β_{aver} is the average of the pixel values inside the same selection box as used in (5) above and σ is the standard deviation of pixel values in an adjacent “flat” area of the image. Since the standard deviation of noise should be preferably measured in a uniform region of an image, it was measured over a uniform adipose or glandular tissue area adjacent to the selected microcalcification. The SNR values are shown in Table III. Combining (5) and (6), we obtain the following definition of the CNR which was used for calculation of the values given below:

$$CNR = (\beta_{hi} - \beta_{low}) / (2\sigma). \quad (7)$$

The results of CNR measurements are shown in Table IV, where, again, each value is an average of the measurements

TABLE II

MICROCALCIFICATION VISIBILITY MEASUREMENTS FOR DARK-FIELD AND BRIGHT-FIELD IMAGES AT DIFFERENT X-RAY ENERGIES AND RADIATION DOSES

Sample ID	X-ray energy (keV)	Mean glandular dose (mGy)	Microcalcification visibility - Coronal Slices		Microcalcification visibility - Sagittal Slices	
			Bright-field	Dark-field	Bright-field	Dark-field
1	32	4	0.25	0.63	0.23	0.51
2	32	8	0.28	0.63	0.26	0.66
2	34	8	0.21	0.60	0.20	0.49
3	32	8	0.26	0.69	0.25	0.55
4	34	4	0.30	0.71	0.26	0.51
5	32	4	0.34	0.77	0.24	0.60
5	32	24	0.23	0.93	0.19	0.80
5	34	4	0.28	0.86	0.22	0.70

TABLE III

SNR VALUES FOR DARK-FIELD AND BRIGHT-FIELD IMAGES AT DIFFERENT X-RAY ENERGIES AND RADIATION DOSES

Sample ID	X-ray energy (keV)	Mean glandular dose (mGy)	SNR - Coronal Slices		SNR - Sagittal Slices	
			Bright-field	Dark-field	Bright-field	Dark-field
1	32	4	6.50	2.06	11.84	3.57
2	32	8	9.74	1.80	24.29	3.63
2	34	8	11.63	1.70	26.95	3.89
3	32	8	13.57	2.00	24.81	3.57
4	34	4	13.38	3.60	19.37	4.04
5	32	4	9.95	2.44	17.56	3.23
5	32	24	19.88	2.90	37.17	3.97
5	34	4	12.19	2.88	18.75	3.33

made for ten different microcalcifications throughout the mastectomy samples at a specific X-ray energy and radiation dose. The results presented in Tables II, III, and IV are discussed in detail in the next section of the paper.

It is instructive to analyze the behavior of the visibility, SNR and CNR as a function of the radiation dose. The visibility, in principle, is supposed to be independent from the dose (see equation (5)). Slight variations of the measured visibility values for different doses in Table II are indeed within the uncertainty margins of the practical measurements. The data in Table III shows that the bright-field SNR, for the same sample and X-ray energy, is approximately proportional to the square root of the dose, as expected in accordance with the theoretical proportionality of the denominator of equation (6) to the inverse of the square root of the number of registered photons (assuming Poisson noise statistics in the images). Note that the inverse dependence here is the result of the flat-field correction of the images [47]. On the other hand, the SNR of

TABLE IV

MICROCALCIFICATION CNR MEASUREMENTS FOR DARK-FIELD AND BRIGHT-FIELD IMAGES AT DIFFERENT X-RAY ENERGIES AND RADIATION DOSES

Sample ID	X-ray energy (keV)	Mean glandular dose (mGy)	Microcalcification CNR - Coronal Slices		Microcalcification CNR - Sagittal Slices	
			Bright-field	Dark-field	Bright-field	Dark-field
1	32	4	1.62	1.30	2.79	1.84
2	32	8	2.79	1.14	6.44	2.42
2	34	8	2.47	1.02	5.34	1.93
3	32	8	3.47	1.39	6.14	1.96
4	34	4	3.92	2.55	5.03	2.51
5	32	4	3.45	1.89	4.26	1.93
5	32	24	4.51	2.69	6.99	3.18
5	34	4	3.40	2.49	4.09	2.36

dark-field images in Table III is consistently low and shows very little dependence on the dose. The likely reasons for this behavior can be found in the Discussion section below.

The dependence of CNR on the dose observed in Table IV is a direct consequence of the equation $CNR = V \times SNR$ and the separate data for the visibility and SNR given in Tables II and III. The bright-field CNR increases with the dose, while the dark-field CNR remains approximately independent of it.

Another important aim of this study was to look at the shape and the size of the microcalcifications in the reconstructed bright-field and dark-field images. Fig. 4 illustrates two microcalcifications in a sagittal slice of the bright-field (a) and the dark-field (b) images. As can be seen in the figure, the microcalcification in the box appears as a single blob in the bright-field image (see Fig. 4 (a)). However, there is a cluster of smaller microcalcifications that are resolved in the corresponding dark-field image, as seen in Fig. 4 (b).

In order to determine which type of image (bright-field or dark-field) is actually more reliable in terms of resolving the true shapes and sizes of the microcalcifications, we looked at a surgical clip contained in one of the mastectomy samples, which has a well-known shape and size. Fig. 5 (a) and (b) show a surgical clip in the bright-field and dark-field images, respectively, of a sagittal slice. As can be seen from this figure, there are some image streaking artefacts around the clip, and also the clip has rounded corners in the bright-field image. The true rectangular shape of the clip is much better resolved in the dark-field image.

Furthermore, we have reconstructed the images without the phase retrieval and also with a smaller δ/β parameter. A related result is shown in Fig. 6. Fig. 6 (a) and (b) are, respectively, the reconstructed bright-field and dark-field PB-CT slices obtained using the methods and parameters described above. Fig. 6 (c) is a bright-field PB-CT slice reconstructed with a smaller δ/β value (equal to 100) and Fig. 6 (d) is a bright-field PB-CT slice obtained without phase retrieval. All these images depict the same microcalcifications outlined by the red boxes. As can be seen from this figure, the microcalcifications in the slices obtained with smaller δ/β parameters (Fig. 6 (c) and (d)) appear somewhat sharper than in the “default” bright-field slice in Fig. 6 (a). However,

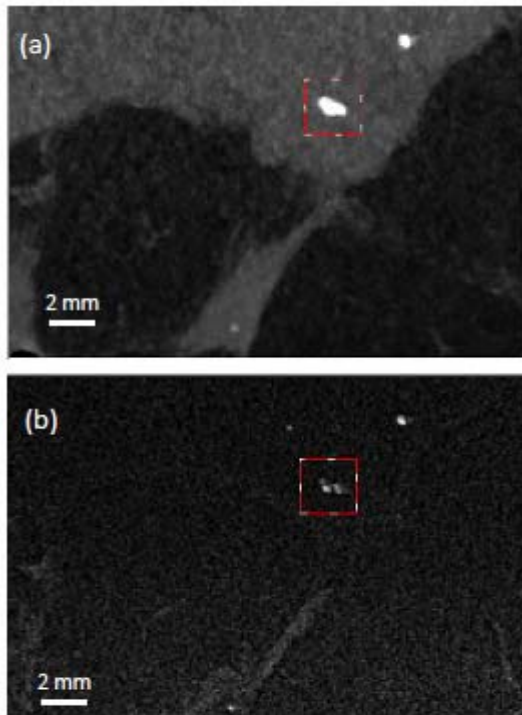


Fig. 4. PB-CT reconstructed (a) bright-field and (b) dark-field images of a sagittal slice of sample 5. The X-ray energy, radiation dose, and sample-to-detector distance were 32 keV, 24 mGy, and 6 m, respectively. Note that the histogram in (a) was adjusted to maximize the visibility of the microcalcifications.

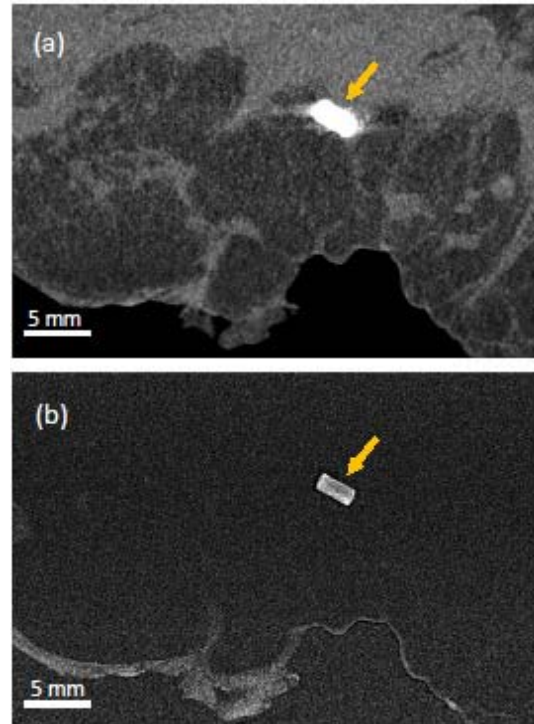


Fig. 5. PB-CT reconstructed (a) bright-field and (b) dark-field images of a sagittal slice of sample 2. The X-ray energy, radiation dose, and sample-to-detector distance were 32 keV, 8 mGy, and 6 m, respectively. The arrow indicates a surgical clip. The histogram in the bright-field image (a) was adjusted to maximize the clip visibility.

Fig. 6 (c) and (d) also have noticeably higher noise compared to **Fig. 6 (a)**, and they still do not show the microcalcifications as well as the dark-field image (**Fig. 6 (b)**).

IV. DISCUSSION

As described in the previous section, we have conducted a study based on our recently proposed method [36] for extracting the dark-field signal in PB-CT imaging datasets to evaluate breast microcalcifications. The analysis of the reconstructed PB-CT dark-field and bright-field images has shown that the microcalcifications can be immediately detected in the dark-field images, without the need for histogram adjustment, as opposed to the bright-field images. An adjustment of the histogram was required in the bright-field images in order to detect some of the microcalcifications embedded in glandular tissue, as illustrated in **Fig. 3**. Having hundreds of images/slices for each mastectomy sample, it could be more efficient for radiologists to look at the dark-field images for microcalcification detection rather than spending time to adjust histograms in the bright-field images.

The visibility of the microcalcifications was also measured at two different X-ray energies (32 keV and 34 keV) and multiple radiation doses (i.e. 4 mGy, 8 mGy, and 24 mGy) for five mastectomy samples with different diagnosis (although not all combinations of the above parameters were available for this study). We have shown, in **Table II**, that the microcalcification visibility in all cases was more than two times higher in the dark-field images compared to the bright-field images. This

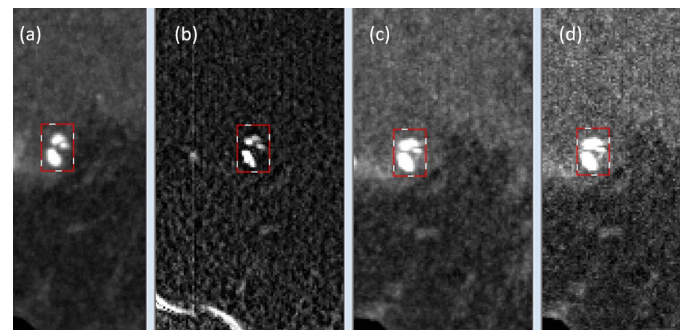


Fig. 6. The same slice through a mastectomy sample reconstructed by different methods. (a) Bright-field PB-CT TIE-Hom reconstruction with $\delta/\beta=300$. (b) Dark-field PB-CT reconstruction. (c) Bright-field PB-CT TIE-Hom reconstruction with $\delta/\beta=100$. (d) Bright-field PB-CT reconstruction without phase retrieval.

was true for both 100 μm thick coronal and 1 mm thick sagittal slices. Another observation was that the calcification visibility was consistently higher in the coronal slices compared to the sagittal slices. This may be due to the fact that in the studied case the coronal slices were ten times thinner than the sagittal slices.

In contrast to the visibility, microcalcification CNR values were lower in the dark-field images compared to the bright-field images as shown in **Table IV**. The reason appears to be related to the average “intensity” in the dark-field images being consistently lower compared to the bright-field images, leading to larger values of the standard deviation in the denominator of (7). Indeed, it is natural to expect the dark-field

signals to be much weaker than the bright-field signal in most real-life scenarios (as fewer photons are usually scattered to higher angles). The lower SNR (as shown in Table III) negatively affected the CNR in the dark-field images in our measurements.

As mentioned in the previous section, the measured SNR in the dark-field images was low and was almost independent of the X-ray dose (see Table III). This phenomenon was related to the method for measuring the SNR employed in our work, which was based on the estimation of noise in flat (featureless) regions of the image. In the case of dark-field images, the flat regions contained very few photons, as there was naturally very little dark-field signal there. Therefore, the SNR measured in these regions of dark-field images was always low at all the tested doses. The observed statistics of the dark-field signal was not Poisson and, in particular, the noise variance was not proportional to the dose. The five samples presented in this paper represent just a fraction of a much bigger set of more than 120 PB-CT scans of full intact mastectomy samples that our group has collected in the course of an experimental program conducted at the Australian Synchrotron over the last five years. The noise behavior discussed here was quite consistent across the images reconstructed from all these PB-CT scans. We hypothesize that the detector dark current may have contributed to the SNR of the measured dark-field signal in a significant way, even though we applied the dark current correction in all our image reconstructions. Unlike the case of the bright-field images, the contribution of the detector dark current to the dark-field images was possibly significant because of the effectively low photon count in the dark-field signal. This question can probably be definitively resolved by using a photon-counting detector (which does not have a dark current) in a similar experiment in the future. We are grateful to the anonymous reviewer for drawing our attention to this possibility.

It is worth mentioning that different samples with the same X-ray energy and radiation dose (for instance samples 1 and 5 both scanned at 32 keV X-ray energy and 4 mGy radiation dose) had different visibility and CNR values (even though the reconstructed mean β values were the same), which can be due to having different types of microcalcifications within the mastectomy samples. As mentioned in the introduction, different types of microcalcifications have different X-ray absorption and dark-field signal (scattering) values. However, with the relatively small number of data points available in the current initial study, we cannot yet confidently claim that the described dark-field imaging method allows one to distinguish between different types of microcalcifications at clinically acceptable radiation doses.

We have demonstrated that the dark-field images can provide more accurate information (compared to the bright-field images) about the size, the shape, and the distribution of microcalcifications within mastectomy samples. Still, as some of our conclusions are based on the analysis of the dark-field images of a surgical clip, and microcalcifications have a different chemical composition from the plastic clip, it would be useful to verify directly (perhaps, by a comparison with histological images) the accuracy of the shape representation

of microcalcifications in PB-CT dark-field imaging in the future. Note, however, that significant difficulties are often experienced when trying to preserve breast microcalcifications in the histological slices. The microcalcifications tend to crumble and often fall out of the tissue when cut by a microtome. This comes in addition to the substantial challenges in co-locating the same regions in 3D between the X-ray CT reconstructions and the histological images of the same breast tissue sample, because of such problems as shearing and distortion of the tissue in the histological sample preparation, different appearance of the image contrast in the optical and X-ray regimes, etc. Therefore, the difficulties in identification and comparison of a detailed shape of a particular microcalcification in an X-ray CT scan and in the histological images should not be underestimated. Since the shape information can help to differentiate between benign and malignant lesions, it can be helpful for the early detection of breast cancer. However, it appears that the bright-field PB-CT images may not be always reliable in terms of classifying microcalcifications. As we have shown in Fig. 4 (a), the reconstructed bright-field image of a sagittal slice depicted a single large microcalcification, which was outlined with a box. However, the reconstructed dark-field image of the same microcalcification revealed a cluster of small microcalcifications, which may be evaluated differently in terms of breast cancer diagnosis. We have shown that the dark-field images are likely to be more reliable in this respect. This suggestion was supported by the evaluation of bright-field and dark-field images of a surgical clip with a known shape, as shown in Fig. 5.

V. CONCLUSION

The results of the study presented in this paper have demonstrated that microcalcifications can be more readily detected in the PB-CT dark-field images compared to the PB-CT bright-field images. Also, a consistently higher microcalcification visibility was measured in the dark-field images compared to the bright-field images for all combinations of X-ray energies and radiation doses. In addition, our experimental data showed that the dark-field images can provide more precise and detailed information about the shape, size, and distribution of microcalcifications compared to the bright-field images. Given that the diagnosis of microcalcification in the absence of additional imaging features (e.g. a mass) is more likely to be DCIS, the challenge is to differentiate microcalcifications without an excess of false positives and thus reduce the number of benign percutaneous biopsies. In this context, the dark-field PB-CT images are likely to help radiologists evaluate the probability of breast cancer more accurately. Future work will be aimed at further refinement of the method and investigation of the possibility to reliably classify different types of microcalcifications using dark-field PB-CT images collected at clinically relevant radiation doses. This work is being conducted in the course of developing a medical imaging facility at the IMBL beamline of the Australian Synchrotron, which will be used for advanced breast cancer imaging, in particular [42], [48]. All the source code that was used for the present study has been made publicly available in GitHub [49].

ACKNOWLEDGMENT

The authors are grateful to the patients who generously allowed their excised post-operative tissues to be used for this study. This research was undertaken on the Imaging and Medical Beamline at the Australian Synchrotron, part of Australia's Nuclear Sciences and Technology Organisation (ANSTO).

A. Aminzadeh is with the School of Physics, The University of Melbourne, Parkville, VIC 3010, Australia (e-mail: aminzadeh@unimelb.edu.au).

B. D. Arhatari is with Australian Synchrotron, ANSTO, Clayton, VIC 3168, Australia, and also with the Department of Chemistry and Physics, La Trobe University, Bundoora, VIC 3086, Australia (e-mail: arhatarb@ansto.gov.au).

A. Maksimenko, C. J. Hall, D. Hausermann, and A. G. Peele are with Australian Synchrotron, ANSTO, Clayton, VIC 3168, Australia (e-mail: antonm@ansto.gov.au; chris.hall@synchrotron.org.au; danielh@ansto.gov.au; andrew.peele@synchrotron.org.au).

J. Fox, B. Kumar, and Z. Prodanovic are with the Faculty of Medicine, Nursing and Health Sciences, Monash University, Clayton, VIC 3800, Australia (e-mail: jane.fox@monash.edu; beena.kumar@monashhealth.org; zdenka.prodanovic@monashhealth.org).

M. Dimmock is with the Department of Medical Imaging and Radiation Sciences, Monash University, Clayton, VIC 3800, Australia, and also with the School of Allied Health Professions, Keele University, Staffordshire, Newcastle ST5 5BG, U.K. (e-mail: matthew.dimmock@monash.edu).

D. Lockie is with Maroondah BreastScreen, Ringwood East, VIC 3135, Australia (e-mail: darren.lockie@unimelb.edu.au).

K. M. Pavlov is with the School of Physical and Chemical Sciences, University of Canterbury, Christchurch 8041, New Zealand, also with the School of Physics and Astronomy, Monash University, Clayton, VIC 3800, Australia, and also with the School of Science and Technology, University of New England, Armidale, NSW 2350, Australia (e-mail: konstantin.pavlov@canterbury.ac.nz).

Y. I. Nesterets and D. Thompson are with the Commonwealth Scientific and Industrial Research Organisation, Clayton, VIC 3168, Australia, and also with the School of Science and Technology, University of New England, Armidale, NSW 2350, Australia (e-mail: yakov.nesterets@csiro.au; darren.thompson@csiro.au).

S. C. Mayo is with the Commonwealth Scientific and Industrial Research Organisation, Clayton, VIC 3168, Australia (e-mail: sherry.mayo@csiro.au).

D. M. Paganin is with the School of Physics and Astronomy, Monash University, Clayton, VIC 3800, Australia (e-mail: david.paganin@monash.edu).

S. T. Taba, S. Lewis, and P. C. Brennan are with the Faculty of Health Sciences, The University of Sydney, Lidcombe, NSW 2141, Australia (e-mail: amir.tavakoli@sydney.edu.au; sarah.lewis@sydney.edu.au; paulick.brennan@sydney.edu.au).

H. M. Quiney is with the School of Physics, The University of Melbourne, Parkville, VIC 3010, Australia, and also with the Faculty of Health Sciences, The University of Sydney, Lidcombe, NSW 2141, Australia (e-mail: quiney@unimelb.edu.au).

T. E. Gureyev is with the School of Physics, The University of Melbourne, Parkville, VIC 3010, Australia, and also with the School of Physics and Astronomy, Monash University, Clayton, VIC 3168, Australia (e-mail: timur.gureyev@unimelb.edu.au).

REFERENCES

- [1] *Australian Cancer Incidence and Mortality (ACIM) Book*, Austral. Inst. Health Welfare, Darlinghurst, NSW, Australia, 2017.
- [2] R. L. Siegel, K. D. Miller, and A. Jemal, "Cancer statistics, 2019," *CA, Cancer J. Clinicians*, vol. 69, no. 1, pp. 7–34, 2019, doi: 10.3322/caac.21551.
- [3] K. Scherer *et al.*, "Improved diagnostics by assessing the micromorphology of breast calcifications via X-ray dark-field radiography," *Sci. Rep.*, vol. 6, no. 1, pp. 1–11, Dec. 2016.
- [4] Z. Wang *et al.*, "Non-invasive classification of microcalcifications with phase-contrast X-ray mammography," *Nature Commun.*, vol. 5, no. 1, pp. 1–9, Sep. 2014.
- [5] A. Fanizzi *et al.*, "A machine learning approach on multiscale texture analysis for breast microcalcification diagnosis," *BMC Bioinf.*, vol. 21, no. 2, pp. 1–11, Mar. 2020.
- [6] J. Li *et al.*, "Diagnostic performance of digital breast tomosynthesis for breast suspicious calcifications from various populations: A comparison with full-field digital mammography," *Comput. Struct. Biotechnol. J.*, vol. 17, pp. 82–89, Jan. 2019.
- [7] K. Thangavel, M. Karnan, R. Sivakumar, and A. K. Mohideen, "Automatic detection of microcalcification in mammograms—A review," *Int. J. Graph. Vis. Image Process.*, vol. 5, no. 5, pp. 31–61, 2005.
- [8] F. Zhang *et al.*, "Cascaded generative and discriminative learning for microcalcification detection in breast mammograms," in *Proc. IEEE/CVF Conf. Comput. Vis. Pattern Recognit. (CVPR)*, Jun. 2019, pp. 12578–12586.
- [9] E. Sakka, A. Prentza, I. E. Lamprinos, and D. Koutsouris, "Microcalcification detection using multiresolution analysis based on wavelet transform," in *Proc. Int. Special Topic Conf. Inf. Technol. Biomed. (ITAB)*, Oct. 2006, pp. 1–4.
- [10] H. D. Cheng, J. Wang, and X. Shi, "Microcalcification detection using fuzzy logic and scale space approaches," *Pattern Recognit.*, vol. 37, no. 2, pp. 363–375, Feb. 2004.
- [11] K. Loizidou, G. Skouroumouni, C. Nikolaou, and C. Pitris, "An automated breast micro-calcification detection and classification technique using temporal subtraction of mammograms," *IEEE Access*, vol. 8, pp. 52785–52795, 2020.
- [12] T. M. A. Basile *et al.*, "Microcalcification detection in full-field digital mammograms: A fully automated computer-aided system," *Phys. Medica*, vol. 64, pp. 1–9, Aug. 2019.
- [13] S. J. Glick, "Breast CT," *Ann. Rev. Biomed. Eng.*, vol. 9, pp. 501–526, Aug. 2007.
- [14] S. Wienbeck, J. Lotz, and U. Fischer, "Review of clinical studies and first clinical experiences with a commercially available cone-beam breast CT in Europe," *Clin. Imag.*, vol. 42, pp. 50–59, Mar. 2018.
- [15] A. Liu *et al.*, "Quantitative breast density measurement based on three-dimensional images: A study on cone-beam breast computed tomography," *Acta Radiologica*, Jul. 2021, Art. no. 028418512110273, doi: 10.1177/02841851211027386.
- [16] S. Wienbeck, U. Fischer, S. Luftner-Nagel, J. Lotz, and J. Uhlig, "Contrast-enhanced cone-beam breast-CT (CBBCT): Clinical performance compared to mammography and MRI," *Eur. Radiol.*, vol. 28, no. 9, pp. 3731–3741, Sep. 2018.
- [17] M. Germann, S. Shim, F. Angst, N. Saltybaeva, and A. Boss, "Spiral breast computed tomography (CT): Signal-to-noise and dose optimization using 3D-printed phantoms," *Eur. Radiol.*, vol. 31, no. 6, pp. 3693–3702, Jun. 2021.
- [18] N. Berger, M. Marcon, T. Frauenfelder, and A. Boss, "Dedicated spiral breast computed tomography with a single photon-counting detector: Initial results of the first 300 women," *Investigative Radiol.*, vol. 55, no. 2, pp. 68–72, Feb. 2020.
- [19] M. Willner *et al.*, "Quantitative breast tissue characterization using grating-based X-ray phase-contrast imaging," *Phys. Med. Biol.*, vol. 59, no. 7, pp. 1557–1571, Apr. 2014.
- [20] P. Coan, A. Bravin, and G. Tromba, "Phase-contrast X-ray imaging of the breast: Recent developments towards clinics," *J. Phys. D, Appl. Phys.*, vol. 46, no. 49, Dec. 2013, Art. no. 494007.
- [21] S. T. Taba, T. E. Gureyev, M. Alakhras, S. Lewis, D. Lockie, and P. C. Brennan, "X-ray phase-contrast technology in breast imaging: Principles, options, and clinical application," *Amer. J. Roentgenol.*, vol. 211, no. 1, pp. 133–145, Jul. 2018.
- [22] R. Longo *et al.*, "Advancements towards the implementation of clinical phase-contrast breast computed tomography at Elettra," *J. Synchrotron Radiat.*, vol. 26, no. 4, pp. 1343–1353, Jul. 2019.
- [23] F. Pfeiffer *et al.*, "Grating-based X-ray phase contrast for biomedical imaging applications," *Zeitschrift Medizinische Physik*, vol. 23, no. 3, pp. 176–185, 2013.
- [24] P. Baran *et al.*, "Optimization of propagation-based X-ray phase-contrast tomography for breast cancer imaging," *Phys. Med. Biol.*, vol. 62, no. 6, pp. 2315–2332, 2017.
- [25] S. Pacilè *et al.*, "Free propagation phase-contrast breast CT provides higher image quality than cone-beam breast-CT at low radiation doses: A feasibility study on human mastectomies," *Sci. Rep.*, vol. 9, no. 1, pp. 1–7, Dec. 2019.
- [26] L. Brombal *et al.*, "Image quality comparison between a phase-contrast synchrotron radiation breast CT and a clinical breast CT: A phantom based study," *Sci. Rep.*, vol. 9, no. 1, pp. 1–12, Dec. 2019.
- [27] G. Mettivier *et al.*, "In-line phase contrast mammography, phase contrast digital breast tomosynthesis, and phase contrast breast computed tomography with a dedicated CT scanner and a microfocus X-ray tube: Experimental phantom study," *IEEE Trans. Radiat. Plasma Med. Sci.*, vol. 5, no. 6, pp. 793–806, Nov. 2021, doi: 10.1109/TRPMS.2020.3003380.

- [28] P. Suortti, J. Keyriläinen, and W. Thomlinson, "Analyser-based X-ray imaging for biomedical research," *J. Phys. D, Appl. Phys.*, vol. 46, no. 49, Dec. 2013, Art. no. 494002.
- [29] P. C. Diemoz, F. A. Vittoria, and A. Olivo, "Spatial resolution of edge illumination X-ray phase-contrast imaging," *Opt. Exp.*, vol. 22, no. 13, pp. 15514–15529, 2014.
- [30] T. E. Gureyev *et al.*, "Refracting Röntgen's rays: Propagation-based X-ray phase contrast for biomedical imaging," *J. Appl. Phys.*, vol. 105, no. 10, May 2009, Art. no. 102005.
- [31] L. Brombal *et al.*, "Phase-contrast breast CT: The effect of propagation distance," *Phys. Med. Biol.*, vol. 63, Dec. 2018, Art. no. 24NT03.
- [32] A. Piai *et al.*, "Quantitative characterization of breast tissues with dedicated CT imaging," *Phys. Med. Biol.*, vol. 64, no. 15, Aug. 2019, Art. no. 155011.
- [33] M. R. Teague, "Deterministic phase retrieval: A Green's function solution," *J. Opt. Soc. Amer.*, vol. 73, no. 11, pp. 1434–1441, 1983.
- [34] D. Paganin, S. Mayo, T. E. Gureyev, P. R. Miller, and S. W. Wilkins, "Simultaneous phase and amplitude extraction from a single defocused image of a homogeneous object," *J. Microsc.*, vol. 206, no. 1, pp. 33–40, 2002.
- [35] T. Rauch *et al.*, "Discrimination analysis of breast calcifications using X-ray dark-field radiography," *Med. Phys.*, vol. 47, no. 4, pp. 1813–1826, Apr. 2020.
- [36] T. E. Gureyev *et al.*, "Dark-field signal extraction in propagation-based phase-contrast imaging," *Phys. Med. Biol.*, vol. 65, no. 21, Nov. 2020, Art. no. 215029.
- [37] L. Frappart *et al.*, "Different types of microcalcifications observed in breast pathology," *Virchows Arch. A Patholog. Anatomy Histopathol.*, vol. 410, no. 3, pp. 179–187, 1987.
- [38] A. W. Stevenson, J. C. Crosbie, C. J. Hall, D. Häusermann, J. Livingstone, and J. E. Lye, "Quantitative characterization of the X-ray beam at the Australian synchrotron imaging and medical beamline (IMBL)," *J. Synchrotron Radiat.*, vol. 24, no. 1, pp. 110–141, Jan. 2017.
- [39] S. T. Taba *et al.*, "Toward improving breast cancer imaging: Radiological assessment of propagation-based phase-contrast CT technology," *Academic Radiol.*, vol. 26, no. 6, pp. 79–89, 2019.
- [40] S. T. Taba *et al.*, "Propagation-based phase-contrast CT of the breast demonstrates higher quality than conventional absorption-based CT even at lower radiation dose," *Academic Radiol.*, vol. 28, no. 1, pp. 20–26, 2021.
- [41] Y. I. Nesterets *et al.*, "A feasibility study of X-ray phase-contrast mammographic tomography at the imaging and medical beamline of the Australian synchrotron," *J. Synchrotron Radiat.*, vol. 22, no. 6, pp. 1509–1523, 2015.
- [42] B. D. Arhatari *et al.*, "X-ray phase-contrast computed tomography for soft tissue imaging at the imaging and medical beamline (IMBL) of the Australian synchrotron," *Appl. Sci.*, vol. 11, no. 9, p. 4120, Apr. 2021.
- [43] K. S. Morgan and D. M. Paganin, "Applying the Fokker–Planck equation to grating-based X-ray phase and dark-field imaging," *Sci. Rep.*, vol. 9, no. 1, pp. 1–14, Dec. 2019.
- [44] D. M. Paganin and K. S. Morgan, "X-ray Fokker–Planck equation for paraxial imaging," *Sci. Rep.*, vol. 9, no. 1, pp. 1–18, Dec. 2019.
- [45] T. E. Gureyev, T. J. Davis, A. Pogany, S. C. Mayo, and S. W. Wilkins, "Optical phase retrieval by use of first Born- and Rytov-type approximations," *Appl. Opt.*, vol. 43, no. 12, pp. 2418–2430, 2004.
- [46] T. Gureyev, S. Mohammadi, Y. Nesterets, C. Dullin, and G. Tromba, "Accuracy and precision of reconstruction of complex refractive index in near-field single-distance propagation-based phase-contrast tomography," *J. Appl. Phys.*, vol. 114, no. 14, Oct. 2013, Art. no. 144906.
- [47] Y. I. Nesterets and T. E. Gureyev, "Noise propagation in X-ray phase-contrast imaging and computed tomography," *J. Phys. D, Appl. Phys.*, vol. 47, no. 10, Mar. 2014, Art. no. 105402.
- [48] D. Häusermann, C. Hall, A. Maksimenko, C. Campbell, and K. K. W. Siu, "The imaging and medical beam line at the Australian synchrotron," in *Proc. AIP Conf.*, 2010, vol. 1266, no. 1, pp. 3–9.
- [49] *PB-CT-DF-Signal*. (Oct. 17, 2021). [Online]. Available: <https://github.com/Alaleham/PB-CT-DF-signal>